

Prediction of the Cu Oxidation State from EELS and XAS Spectra Using Supervised Machine Learning

Samuel P. Gleason^{1,2*}, Deyu Lu³ and Jim Ciston^{1*}

¹National Center for Electron Microscopy Facility, Molecular Foundry,
Lawrence Berkeley National Laboratory, Berkeley, CA, USA.

²Department of Chemistry, University of California, Berkeley, 94720,
CA, USA.

³Center for Functional Nanomaterials, Brookhaven National Laboratory,
Street, Upton, 100190, NY, USA.

*Corresponding author(s). E-mail(s): smglsn12@berkeley.edu;
jciston@lbl.gov;

Abstract

Electron energy loss spectroscopy (EELS) and X-ray absorption spectroscopy (XAS) provide detailed information about bonding, distributions and locations of atoms, and their coordination numbers and oxidation states. However, analysis of XAS/EELS data often relies on matching an unknown experimental sample to a series of simulated or experimental standard samples. This limits analysis throughput and the ability to extract quantitative information from a sample. In this work, we have trained a random forest model capable of predicting the oxidation state of copper based on its L-edge spectrum. Our model attains an R^2 score of 0.89 and a root mean square valence error of 0.21 on simulated data. It has also successfully predicted experimental L-edge EELS spectra taken in this work and XAS spectra extracted from the literature. We further demonstrate the utility of this model by predicting simulated and experimental spectra of mixed valence samples generated by this work. This model can be integrated into a real time EELS/XAS analysis pipeline on mixtures of copper containing materials of unknown composition and oxidation state. By expanding the training data, this methodology can be extended to data-driven spectral analysis of a broad range of materials.

Keywords: Machine Learning, EELS, XAS, Cu, Spectral Analysis

Introduction

Due to their wide range of accessible oxidation states and materials applications, the ability to determine the oxidation state of third row transition metals is essential to a wide variety of applications. These include the development of catalysts [1], photovoltaic devices [2], and biotechnology [3]. Core level spectroscopy is often used to probe transition metal oxidation states, and two main types are electron energy loss spectroscopy (EELS) and X-ray absorption spectroscopy (XAS). EELS provides detailed atomic scale information, such as oxidation state, coordination number and local symmetry of a nanomaterial [4, 5]. When probing nanomaterials, EELS is often combined with scanning transmission electron microscopy (STEM). In STEM-EELS, an electron beam is scanned over an area of a sample and a full spectrum is acquired and stored at each probe position. This technique is particularly valuable in the study of nanomaterials due to its combination of high spacial and high energy resolution. [6–8]. Like EELS, XAS has also attained wide usage in determining oxidation state and local environment in nanomaterials [9–11]. XAS, however, is typically limited to a spacial resolution of a few nanometers [12], rather than the sub angstrom spacial resolution possible with STEM-EELS [13]. The main advantages of XAS compared to EELS for core-loss spectroscopy are the ability to attain higher signal to noise ratios (SNR) and higher energy resolution, particularly at higher excitation energies [14], and functionality on thicker samples for hard x-ray excitation [15]. Due to the myriad use cases for both techniques, they are commonly applied to the nanoscale study of materials containing third row transition metals. However, since EELS and XAS spectra encode the electronic properties of the sample in an abstract way, extracting physical descriptors is a non-trivial task in spectral analysis.

Therefore, quantitative spectral analysis is often the rate limiting step in materials characterization, and can typically only be conducted by trained experts. This is especially true of L-edge spectra of transition metals, where variations in oxidation state can manifest in small shifts in edge location, L_2/L_3 ratio and peak width that are not immediately obvious to a non expert, particularly for samples containing multiple oxidation states [16]. Oxidation state assignment is typically done by mapping the unknown spectrum to known experimental or simulated standards, a process which can be time intensive and requires significant domain knowledge. Particularly challenging to analyze are mixed valence materials, which are often interpreted as combinations of spectra of integer valence structures [17]. The prevailing solution to this problem is to fit integer valence spectra to the unknown spectrum using least squares. This allows a user to input known standards and determine the coefficients of a linear combination of the standard spectra that reproduce the experimental spectrum [17–20].

Least squares fitting has allowed quantitative oxidation state analysis of mixed valence samples, and is widely implemented as the state-of-the-art procedure for quantitative analysis of unlabeled XAS/EELS L-edge data. However, in the case of experimental standards, it has a few serious limitations. First, this procedure requires fresh standards to be taken for each instrument, and often each day, as changes in detector setup and alignment can lead to non trivial changes in the spectra. Second, this procedure is highly sensitive to experimental variation in the acquisition of the

standard samples. Contamination with materials of other oxidation state, surface oxidation and beam damage can have a significant impact on the shape of the standard spectrum, and therefore interfere with the fitting of the unknown sample. Additionally, inconsistencies in standard spectrum processing, such as baseline subtraction or the incomplete deconvolution of multiple scattering from the standard sample, can have a similar impact. Third, the presence of any oxidation state or coordination environment unaccounted for by the standards will not only be missed by the prediction of the makeup of the material, potentially missing an important fundamental discovery, but will also lead to an inaccurate representation of the oxidation state as the standard components are forced to represent a signal not originating from any of them. In a similar vein, experimental standards must be taken for every material expected to be present in order to perform the oxidation state analysis. For example, a standard for CuO may not be suitable for an experiment involving CuS due to non trivial differences between the spectra, although they are both a Cu(II) oxidation state [21, 22]. Simulated standards suffer from fewer experimental limitations, but instead are limited by the level of approximations used in the theory and often can not perfectly reproduce experimental spectra. This can cause systematic errors leading to significant misidentifications, particularly when applied to noisy experimental spectra or experimental spectra more challenging to simulate. It is rare for simulated standards for L-edge transition metal spectra to be quantitatively accurate enough to fit an unknown experimental spectrum using least squares fitting [23]. Instead, these are used to qualitatively match components of an unknown spectrum. Therefore, there is a need for a procedure that can determine oxidation state from XAS/EELS L-edge data that is more robust than the least squares fitting of a handful of standard spectra.

An avenue for a more broadly applicable automated analysis procedure is machine learning (ML). Despite some recent advancements in automated L-edge XAS/EELS analysis of transition metals using ML approaches [24], overall, the transition metal K-edge has received more focus from the ML community [25–27]. Numerical analysis of L-edge transition metal XAS/EELS data has mainly been performed using principle component analysis (PCA) to reduce the dimensionality of the spectrum. This field has been well developed, comprising numerous applications of PCA on L-edge XAS/EELS data [28–31]. Additionally, PCA dimensionality reduction procedures have been used to successfully de-noise low SNR core loss EELS data [32–34]. PCA has also been extended into analysis of oxidation states. Applying component analysis to a mixed valence XAS/EELS spectrum can result in components that mimic the unique oxidation states present. This can be used as a qualitative estimation of the different oxidation states present in a sample, however, it is difficult to ensure each of the resulting components match the pure form of an oxidation state. Therefore, the lack of rigorous physical interpretation of the components makes any quantitative analysis challenging [35].

Supervised machine learning approaches have found success predicting oxidation states in manganese and iron samples, using neural networks and support vector machines [36–38]. However, these models were trained on a small subset of materials and, with the exception of [37] on Mn spectra, only focused on integer valence states. Therefore, the more complicated question of L-edge spectra oxidation state regression

of an arbitrary Cu material containing a wide range of oxidation states has not been thoroughly explored. The lack of focus on mixed valence structures generally is especially notable, as such a model is necessary to analyze an in-situ experiment where 1000s of spectra are generated quickly with minor variations in oxidation state.

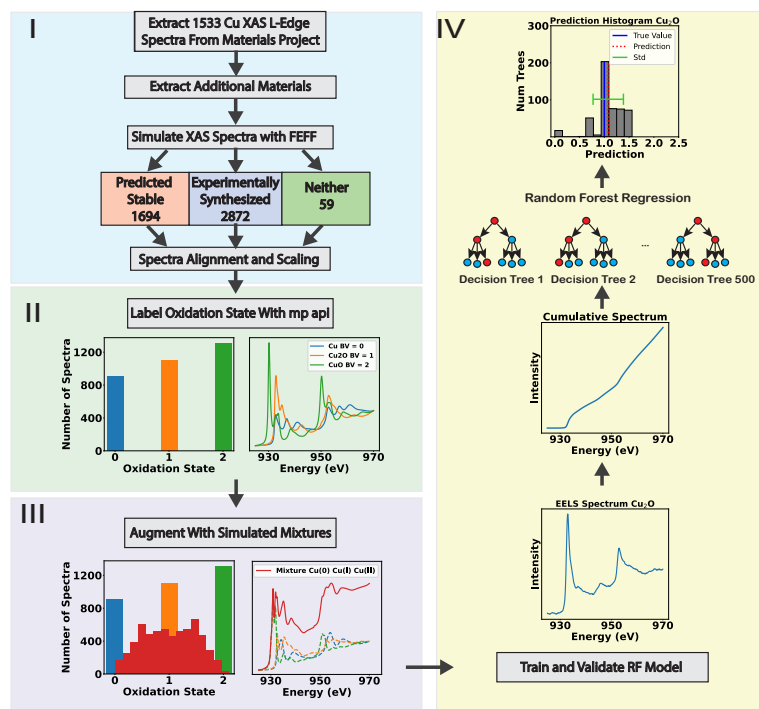


Fig. 1 A flow chart containing the four components of constructing the training data and random forest model. First, data is extracted from the Materials Project and scaled, aligned and processed to ensure internal consistency and accuracy to experiments. The colored boxes in I show how the materials project classifies the materials extracted and simulated by this work. Second, the spectra are labeled by their oxidation state using the Materials Project oxidation state function "get valence". Third, the dataset is augmented by creating mixture spectra made up of linear combinations of integer valence spectra. Fourth, the random forest model is trained and validated using test simulated data and experimental reference samples [39].

This work has developed a supervised ML model capable of conducting a regression task on an unlabeled Cu $L_{2,3}$ -edge XAS/EELS spectrum and predicting the average oxidation state. The $L_{2,3}$ -edge was selected as the focus due to the prohibitively high energy of the transition metal K-edge for electron detectors. We utilized the simulated L-edge XAS spectra of transition metals stored in the Materials Project [39, 40] as a seed to construct our training set. Despite the differing physical origins of XAS vs EELS, with XAS caused by excitation from a photon and EELS by an electron, under

the long wave-length limit and dipole approximation, both spectroscopic methods involve evaluating the same transition matrix element. Therefore, a model trained on XAS data is able to effectively predict EELS data [41, 42] for features where the quadrupole contribution is not significant.

Cu was selected as the focus of this work due to the myriad applications of Cu nano-materials. Specifically, Cu nanoparticles (CuNPs) are used in antimicrobial agents [43], catalysts [44] and renewable energy devices, particularly the electrochemical reduction of CO_2 [45]. Examining the oxidation state of Cu nanomaterials is critical to their function, as CuNP preparation procedures can lead to unintended surface oxidation that disrupts many of their applications [43]. Additionally, the major trends in Cu L-edge spectra can be captured accurately in Cu metal, Cu_2O and CuO using the multiple scattering¹ method implemented in the FEFF9 code [40, 46]. Figure S1a-c shows good agreement in the L_2 - L_3 spacing and well preserved intensity ratios between the L_2 and L_3 peaks. Fine detail such as the splitting of the L_3 peak in Figure S1a is demonstrated as well. The limitations of this method include the treatment of the partially filled $3d$ bands in Cu(II), where the many-body effects, such as multiplet effects, require higher levels of theory beyond the mean-field level [23, 46]. This can produce some spurious artifacts in the simulations, such as the L_3 shoulder in the CuO simulation (Figure S1c) which is not present in the experimental sample. Although the quadrupole contribution can play an important role in pre-edge features, distinct spectral features in the main edge regions are found to be sensitive to the oxidation state from feature importance analysis. Therefore, neglecting the quadrupole contribution will not have a significant impact in this analysis. The overall success of FEFF9 in producing Cu L-edge spectra allows Cu materials to serve as a model system for this type of automated analysis procedure. In this work we present a framework for predicting the Cu oxidation state that can be readily extended to other transition metals by acquiring a volume of corresponding simulated XAS data.

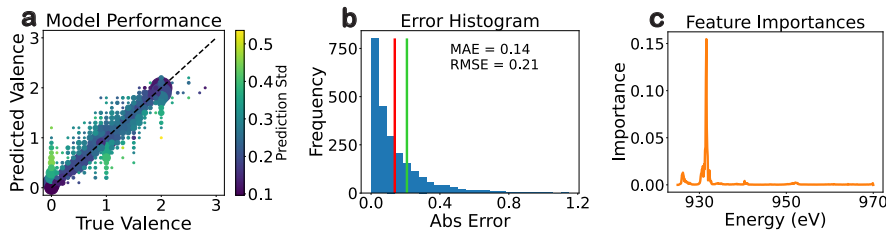


Fig. 2 The performance of the random forest model on the test set of simulated data. (a) R^2 plot, where each spot’s size is proportional to the number of spectra at that point and its color corresponds to the prediction’s standard deviation. (b) histogram of the absolute errors, with the vertical green line showing the location of the root mean square error (RMSE) and the vertical red line showing the location of the mean absolute error (MAE). (c) feature importance of the random forest model plotted on the same energy axis as the spectra.

¹In this case multiple scattering refers to the interference of multiple scattering paths, not to be confused with sequential inelastic events originating from the same excitation source.

Results and Discussion

Performance on Simulated Spectra

Our RF model shows a high level of accuracy on a test set of simulated data. Figure 2a shows the R^2 plot of the predictions of this test set, which contains roughly 2400 spectra. The R^2 for this model is 0.89, and shows a visible high degree of correlation across all the well represented oxidation states. The largest errors come from integer valence misprediction, most commonly when a Cu(0) or Cu(I) spectrum is predicted as mixed valence. However, as shown in Figure 2a, these mispredictions can often be differentiated from the accurate predictions by using the prediction standard deviation (described in the methods section). The feature importance plot from Figure 2c offers insights into the origin of these errors. The model takes a small amount of information from the pre-edge and then bases its prediction mostly on the location and shape of the L_3 peak. As Cu(0) and Cu(I) have L_3 peaks at almost exactly the same energy, these are harder to differentiate than Cu(II), which is red shifted by roughly 3 eV. Despite this difficulty, Cu(0) and Cu(I) are accurately identified far more often than they are mispredicted, as shown in Figure 2a. As can be seen from Figure 2b, a full integer miss, i.e. a Cu(0) spectrum incorrectly called a Cu(I) spectrum, essentially never occurs. What is even more encouraging in Figure 2a and 2b is the simulated mixture samples are frequently predicted with a high degree of accuracy, showing this model has significant potential in predicting mixed valence samples. Figure S5 shows the model’s prediction on the individual spectra used to build the mixed valence dataset, and illustrates that they are a representative sample of our integer spectra, comprising many spectra predicted accurately with a small number of larger misses between Cu(0) and Cu(I). It should be noted that the construction of the mixture dataset occurred before model training. Therefore, the random split of the entire dataset, including mixtures, between training and testing data placed some of the individual integer oxidation state spectra visualized in Figure S5 in the augmented mixed-valent training set. In no cases were the same mixed, or integer, spectra present in both the training and test sets.

Model Uncertainty Metric

In this work we have developed a method for quantifying the uncertainty in our RF model’s prediction. This is done by examining the predictions of each of the 500 decision trees which comprise the random forest as well as the averaged value used as the final prediction. This uncertainty analysis is visualized by generating a prediction histogram, as shown in Figure 1 (IV) and Figure 3d-3f. Beyond the qualitative spread of predictions shown in the prediction histograms, the uncertainty can be understood quantitatively by calculating the standard deviation of these predictions. This is indicated by the horizontal green line in the prediction histogram plots shown in Figures 1 and 3, and is used here as the RF model’s internal uncertainty measurement. To leverage this quantitative uncertainty, the standard deviation can be used to filter out predictions that are highly uncertain, and therefore presumably less accurate. Figure S6 illustrates this concept, where a standard deviation threshold was imposed, and

all predictions with a standard deviation higher than this value were discarded due to their high uncertainty. The standard deviation can be used as a powerful tool in determining significantly inaccurate predictions on simulated data, as can be seen when the threshold is set at 0.35 (red rectangle in Figure S6a and S6b). When this threshold is used, 9% of the predictions of our test set are higher than the threshold and discarded (Figure S6a). However, imposing this threshold causes the RMSE of the remaining 91% of our test set to decrease 20% from the full test set value of 0.21 to 0.17 (Figure S6b). Therefore, the 9% of the test set discarded by this method is comprised of predictions less accurate than average by a significant margin, showcasing the utility of this uncertainty metric in informing the accuracy of the model's predictions for unknown samples.

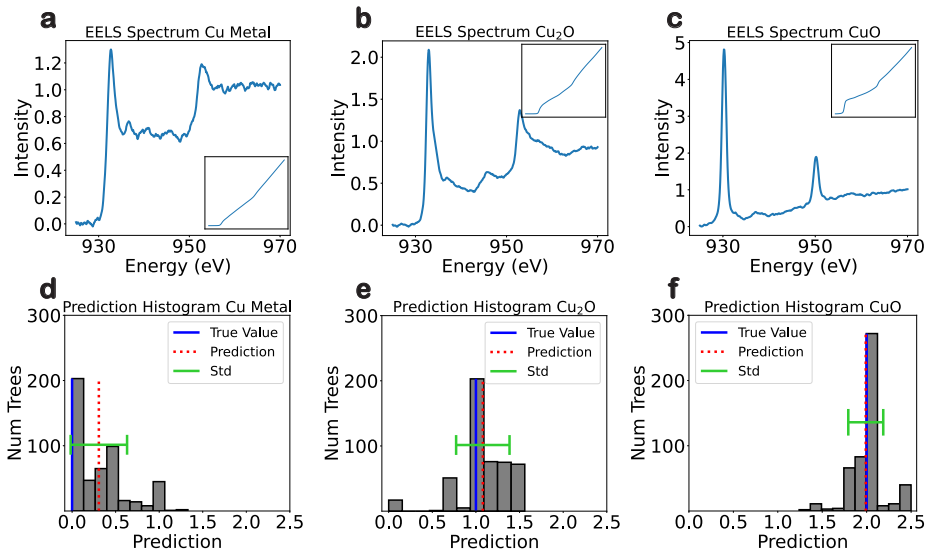


Fig. 3 The performance of the random forest model on experimental Cu oxide EELS standards collected in this work. The top row (a, b, c) shows the raw spectrum with the cumulative spectrum as an insert. The bottom row (d, e, f) shows the prediction histograms for each spectrum, where the grey bars correspond to the number of decision trees predicting values over that range, the red dashed line shows the prediction, the blue solid line shows the labeled value, and the green horizontal line shows the standard deviation of the individual decision trees predictions.

Validation Using Experimental Spectra

To test the RF model's validity when applied to experiments, we used the model to predict a set of metallic Cu and Cu oxide standards. The simulated spectra corresponding to these standards were left out of both the training and test sets previously discussed. These standards were smoothed using a Savitzky-Golay filter with a window size of 1.5 eV and a polynomial order of 3. From Figure S10 it can be seen that the

level of smoothing makes virtually no difference in prediction accuracy, with the only small difference coming from Cu(0), which is likely due to the high level of noise in the raw spectrum of that sample (Figure S7). The smoothing window of 1.5 eV was selected as the default method due to observations that it removed the vast majority of the noise but also preserved the overall shape of the spectrum. From Figure 3e and 3f it can be seen that the model has a high degree of accuracy when predicting Cu(I) and Cu(II), rendering essentially perfect predictions for each of these standards. However, Figure 3d shows the Cu(0) standard appears to be slightly over estimated, as it is predicted at roughly 0.3. There are likely two factors responsible for this observation. First, as has been discussed above, random forest models average predictions across individual decision trees, in this case 500. Therefore, it will always be more challenging for this model to predict Cu(0) as exactly zero, as all materials have non-negative valence. Consequently, any spread in the predictions will result in an overestimate. It is worth noting that in Figure 2a this issue rarely manifests in our predictions on test simulated data. However, due to increased uncertainty around experimental spectra due to minor differences between the experimental and simulated spectra, it is not unreasonable to suspect this feature could prove to be a greater factor when applied to experiments. It is also worth noting that Figure 3d shows that the mode of our prediction histogram is Cu(0) by a factor of two over the next highest bar. Additionally, a second factor may also partially explain this overestimate, which is that our Cu(0) likely experienced some surface oxidation. Therefore, it may be assumed that this material no longer had a true oxidation state of zero at the time of measurement. This is reflected in the spectrum, which can be seen to have visibly taken on some additional Cu(I) character relative to simulated Cu(0) and Cu(0) observed in XAS studies taken from the literature (Figure S8, [21]) Therefore, we believe that this prediction of a mixed valence material closer to Cu(0) than Cu(I) matches our experimental realities and a detailed examination of the experimental spectrum.

Given that the edge position of our training data has been manually aligned to our experimental spectra, it is reasonable to inquire how significant an impact an energy misalignment will have. To explore this, we created a set of experimental spectra where the onset energy was shifted by controlled amounts and tracked how this shift impacted the oxidation state prediction (Figure 4). From Figure 4a we see that the energy misalignment has the greatest impact on the Cu(0) sample, and an offset of greater than -0.2 eV causes an inflection point where the prediction jumps from 0.3 to nearly 0.5. Interestingly, misalignment in the positive direction has a far less dramatic impact, and an energy shift of +0.5 eV produces essentially no change in the prediction. The opposite trend is observed in the Cu(I) sample from Figure 4b, where a negative shift produces little change in the prediction, while an inflection point occurs with a positive shift of greater than +0.2 eV. In Figure 4c, however, we see that Cu(II)'s prediction is virtually independent of shift plus/minus 1 eV, which is likely explained by the greater than 2 eV gap between the onset energy of Cu(II) vs Cu(I) and Cu(0).

To further examine the utility of our model when applied to experimental spectra, and to further study the impact of absolute energy shift on a model that was aligned to our experimental samples, an additional experimental validation was done using an extracted set of XAS spectra of Cu oxides [21]. This set of spectra has been measured

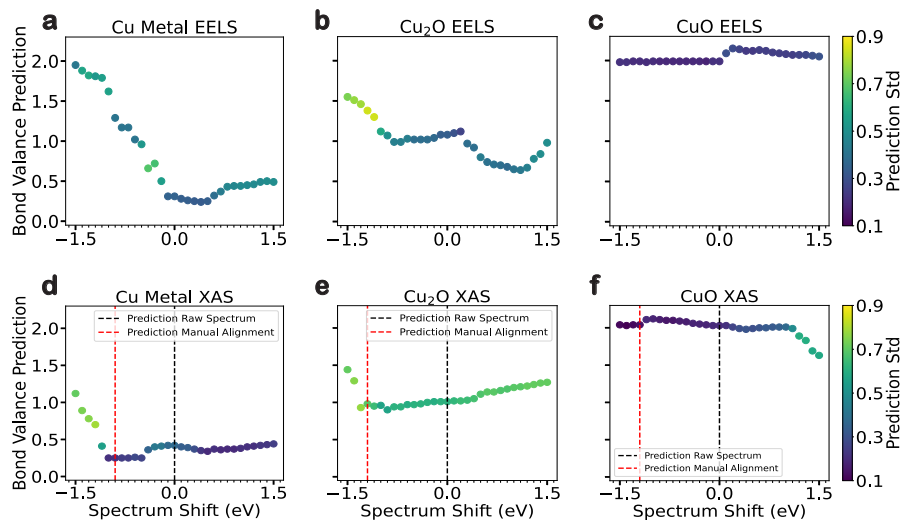


Fig. 4 The impacts of energy misalignment on the prediction for EELS spectra taken in this work (a, b, and c) and XAS spectra extracted from the literature (d, e, f) [21]. The spectra are shifted horizontally on the energy axis by the amount indicated in the x axis but are not changed in any other way. The scatter plot color corresponds to the prediction’s standard deviation.

to be -0.9 eV for Cu metal and -1.2 eV for Cu_2O and CuO (Figure S1) shifted from the experimental spectra used to validate this model, and provides a test case for how the model will respond to spectra with their energy axes significantly misaligned. From Figure 4d-f, we can see that our ML model produces excellent results for the XAS spectra when they are correctly aligned to our training data (red line in Figure 4d-f) and the results are robust even when the raw spectra are predicted, which are severely misaligned (black line in Figure 4d-f). When such a misalignment has occurred, the Cu(I) and Cu(II) spectra are predicted with near perfect accuracy, while the Cu(0) spectrum appears to be slightly over estimated, returning a prediction of 0.4 when the correct alignment prediction is 0.25. It is worth reflecting this prediction is still a slight overestimate, although closer to zero than our experimental EELS spectrum shown in Figure 3d, reflecting this model’s slight propensity to overestimate Cu(0). With these observations, it is clear that the ML model trained on properly aligned spectra can achieve highly accurate results on spectra with significant energy misalignment. Additionally, a potential avenue to determine the true alignment location is to vary the energy axis and seek out regions of consistent stability and low prediction standard deviation, as these regions are clearly associated with more accurate predictions for all our experimental data.

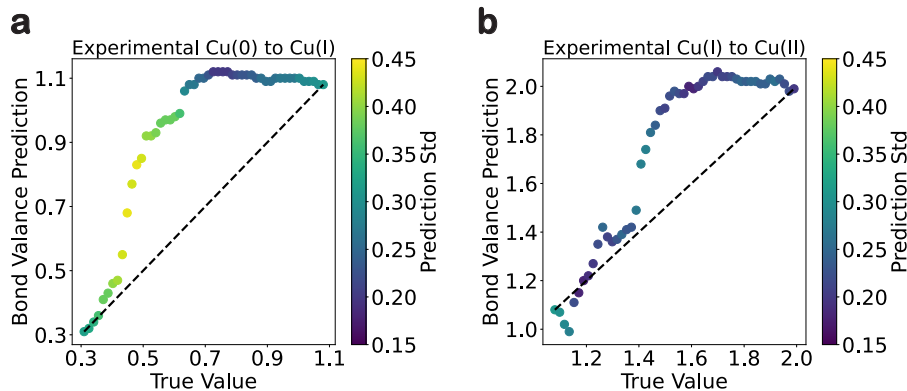


Fig. 5 Performance of the random forest model on experimental mixed valence spectra. (a) mixtures of Cu(0) and Cu(I), while (b) shows mixtures of Cu(I) and Cu(II). The scatter plot color corresponds to the prediction’s standard deviation. The dashed line indicates the location of a perfect prediction.

Prediction of Experimental Mixed Valence Samples

Post successful proof of concept for our model on standard experimental samples, we turn our attention to a more valuable, but also more challenging, experimental case, samples of mixtures of different oxidation states. As shown in Figure 2a, our model has already demonstrated a high degree of accuracy on simulated mixed valence samples. Additionally, we show how smooth variance in simulated mixed valence materials excluded from the training data is captured by our model by showing simulated mixtures of Cu(0), Cu(I) and Cu(II) in Figure S7. The important test for the utility of this model in experimental spectra is how well this process works on experimental mixtures of oxidation states. Due to the difficulty in engineering a system with smoothly varying mixed valence states, and inherent uncertainties in quantifying such a system, we have generated mixed valence experimental spectra through linear combinations of our standard samples. The labeled value for these experimental mixtures is determined by multiplying their oxidation state by their contribution to the final mixture spectrum, as was done with the labeling for the simulated mixtures. However, in this case, the labeled oxidation state for the standard samples was taken to be the prediction shown in Figure 3, rather than the nominal value. For example, a mixture of 40% Cu(0) standard and 60% Cu₂O standard would be calculated as follows:

$$0.31 * 0.4 + 1.08 * 0.6 = 0.772 \quad (1)$$

This is because our model predicts the Cu(0) standard to be 0.31 and the Cu₂O standard to be 1.08 and, as has already been mentioned above, we consider this mixed valence value for our Cu(0) to be more representative than a label of zero valence. The results are shown in Figure 5. From Figure 5a-b, we see both plots contain regions of high accuracy, particularly for mixtures of Cu(I) and Cu(II) (Figure 5b). These mixtures are accurately predicted to within less than 0.1 in around half of the mixture

samples. However, we can see that the absolute accuracy has sections of low accuracy, particularly at inflection points where the prediction is changing quickly. This is particularly true for mixtures of Cu(0) and Cu(I) (Figure 5a), where the inflection region drives the prediction into a region of overestimation which is not recovered until the mixture becomes entirely Cu(I). However, the overall trend of the prediction is correct, as in both Figure 5a and b the higher valence sample is identified as such until a pure sample is predicted, regardless of any absolute inaccuracies in the prediction. Both mixed valence cases tend overestimate the oxidation state when the higher oxidation state sample comprises greater than 50% of the mixture. Likely due to the similar locations of the L_3 peaks for Cu(0) and Cu(I), it has particular trouble differentiating nearly even mixtures of these materials. For future work, it is possible to introduce an additional empirical correction to the RF model’s prediction based on the trends in Figure 5.

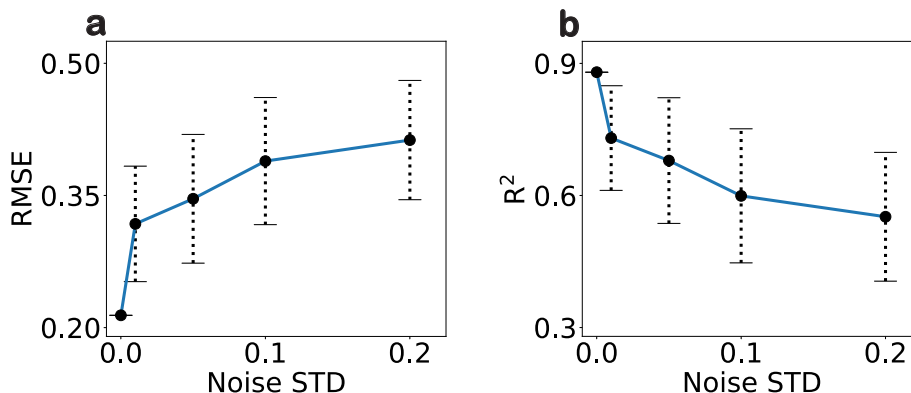


Fig. 6 Random forest model performance on simulated data augmented by Poisson noise. The standard deviation of the Poisson distribution used to generate the noise is shown in the x axis of each plot. The error bars denote the standard deviation of the RMSE/ R^2 across 100 random states for that noise standard deviation value.

Impact of Noise on Simulated Data

To test the impact of noise on the simulated data, random Poisson noise was added to each simulated spectrum in the test set to produce a test set augmented by noise. To ensure that this process echoed our approach on experimental spectra as much as possible, the simulated spectra, which are on a 0.1 eV resolution, were re-sampled using scipy’s 1d interpolation function with a higher resolution of 0.03 eV, matching that of our experimental samples. Noise was then added to the interpolated spectra, and these spectra were then smoothed in the same method as the experimental spectra and integrated to produce a cumulative spectrum (Figure S7). These spectra were then predicted by the model to test its accuracy on noisy data.

As shown in Figure 6a, the simulated data are relatively sensitive to noise augmentation, and the addition of a small amount of Poisson noise resulted in an increase in RMSE from 0.21 to 0.3 as compared to results from the noiseless spectra. Further increase in noise led to an even larger RMSE, however the decline in accuracy becomes less sharp than the initial slope. A similar trend is seen in Figure 6b for R^2 , where a drop in R^2 is observed after adding a small amount of noise, however this decline is less sharp than the increase in RMSE, and adding additional noise has a more pronounced decline on R^2 than subsequent noise does on RMSE. Despite this observation, the noise level of our experimental spectra, which are noticeably larger than the simulated low noise case, do not appear to suffer as much as these simulated noisy spectra (Figure S7). Additionally, the selection of the random seed for the addition of noise appears to have a significant impact on the overall accuracy of the noisy test set. This is shown with the error bars in Figure 6a and 6b, which represent the standard deviation across 100 different random noise seed states. The presented RMSEs and R^2 s are the average values across these 100 random states. A detailed examination of the noise profiles for these higher error random states shows that in these spectra the region around the baseline experiences noise spikes that mimic features around the baseline region, similar to how an inaccurate power law subtraction of an EELS spectrum baseline appears. This observation further enforces that the accuracy of this model relies heavily on the accurate identification and subtraction of the baseline.

Conclusion

In this work, we have built a random forest model trained on simulated L-edge XAS spectra which is capable of predicting the oxidation state of copper based on its L-edge XAS/EELS spectrum. We have also developed a database of Cu XAS spectra containing 3500 unique materials that have been accurately aligned to experimental spectra, and augmented this database with 6000 simulated mixture spectra. Our random forest model attains an R^2 of 0.89 on simulated data with an RMSE of 0.21 and has been shown to accurately predict experimental spectra taken from our home institution and from the literature. Additionally, this model has proven successful predicting mixed valence samples, showing its applicability to track Cu oxidation state in in-situ experiments where oxidation state is changing fluidly as a reaction occurs. Beyond this model’s utility to Cu materials, we have also developed a broader methodology which can be extended to the analysis of other materials by acquiring a spectral database of accurate simulated L-edge spectra for the corresponding material.

Methods

Training Set Generation

In this work, simulated FEFF9 XAS spectra of Cu materials were extracted from the Materials Project. This initial extraction produced a dataset of site averaged spectra for 1533 materials, which contains the 59 materials shown in Figure 1I labeled as neither predicted stable nor synthesized [40]. To increase the volume of our training data, an additional 2000 structures were selected by searching the Materials Project

for all Cu containing materials that had either been previously synthesized or were predicted to be stable by theory [39]. This choice screens a broad material space that is likely accessible to experiments. We computed 2000 site averaged spectra using the *Lightshow* workflow [47] and FEFF9 [46]. The combination of this augmentation step and the initial extraction of L-edge spectra already generated by the Materials Project provided 1199 materials that both have been experimentally synthesized and are predicted to be stable (Figure 1I). For each structure, unique Cu sites are determined by the space group symmetry. Then site specific spectra were calculated using FEFF9. The L_2 and L_3 spectra for each site were combined into the $L_{2,3}$ spectrum by summing the L_2 and L_3 spectra, after first interpolating onto the same energy grid (Figure S2). The site averaged spectrum is calculated from the weighted sum of site-specific spectra based on the multiplicity of the unique sites in the unit cell. The oxidation state of the site specific spectra were determined using the Materials Project’s “get valences” function [39]. Despite this averaging procedure, greater than 93% of the site averaged spectra retained integer valence. When FEFF9 failed to converge for some, but not all, of the sites in a material, converged site spectra were averaged leaving out the failed spectra.

To prepare our training set of 3500 site averaged spectra, several additional steps were performed. This workflow is summarized in Figure 1. First, spectra were interpolated to ensure they were all on a 0.1 eV energy resolution. Second, the non uniformity in the energy range of the L_3 edge, specifically at the starting point, was addressed by fitting a 6th order polynomial to connect the lowest energy point to [925, 0] (i.e., vanishing intensity at 925 eV) for every spectrum (see Figure S3). The spectra were then aligned to ensure their onset edges matched those seen by experimental EELS Cu materials, as it was observed that there was a systematic misalignment occurring in the absolute energy of the $L_{2,3}$ edge.

To accomplish this alignment, two systematic errors were corrected. First, a high degree of onset energy variability was observed within an oxidation state, especially for zero valence materials. Second, the absolute energy of the simulated spectrum was several eV off from experimental standards. Both of these issues were fixed simultaneously by our automated alignment procedure. By subtracting the predicted Fermi energy from the simulated spectra and adding an experimental reference energy taken from our home instrument, correct energy alignments across the three main oxidation states for Cu materials, Cu(0), Cu(I) and Cu(II) were established. The experimental reference energies were obtained using three reference standards (Cu metal, Cu_2O , and CuO) taken in this work, and the same shift values were used for all materials with the same oxidation state in our spectral database. For the small subset of materials that were classified as mixed valence, they were aligned based on whichever integer oxidation state they were closest to.

Our spectral dataset was then augmented by generating simulated mixed valence samples (see step III in Figure 1, Figure S4). To accomplish this, 300 random sets of spectra were drawn from the integer dataset, each draw taking a random Cu(0), Cu(I) and Cu(II) site averaged spectrum. Each of these 300 sets of 3 integer spectra were then linearly combined to mimic mixed valence structures. For each set of three spectra, 20 random fractions of each material were combined to produce a simulated

mixed valence spectrum. To ensure an even spread of mixed valences, 100 sets were combinations of Cu(0) and Cu(I), 100 were combinations of Cu(I) and Cu(II), and 100 were combinations of Cu(0), Cu(I) and Cu(II). This mixture produced a final dataset of roughly 9500 spectra with data well distributed from Cu(0) to Cu(II) (step III in Figure 1, Figure S4).

To achieve the best ML model performance, we have tested different spectral representations, including the spectrum itself, its first and second derivative, and the cumulative integral of the spectrum. We found that the best model performance was achieved with the cumulative integral with intensity normalized to 1. In addition, using the cumulative integral, referred to as a cumulative spectrum from this point on, as input feature can ensure consistency in the absolute scale of the EELS spectrum. This representation can simplify intensity scaling, as experimental post processing decisions and noise can create a high degree of variability in spectral intensity. The cumulative spectrum approach is insensitive to the absolute scale of the spectrum, although it does require an accurate identification and subtraction of the baseline for experimental spectra.

Random Forest Modeling

Random forest (RF) models for this work were trained using Scikit-learn’s RandomForestRegressor model [48]. The number of trees was fixed at 500, with all features available and max depth unfixed. The dataset was split into train and test components using a 75/25 random train test split function from Scikit-learn. The structure of this model allows for the input of a raw spectrum of arbitrary min and max energy and energy scale. The model then takes the input spectrum and interpolates it to a 0.1 eV resolution from 925 to 970 eV to ensure the consistency of the energy grid used in the training data. Spectral smoothing is then applied using a Savitzky-Golay filter from scipy [49]. The smoothing step is done before the interpolation provided that the inputted spectrum is on an evenly spaced energy scale. The cumulative operation on the spectrum is then performed and this spectrum is the input of the model. The trained RF model is an ensemble of 500 individually trained decision trees, and returns the predictions of each decision tree. A simple average of inferred valence values from each tree is taken as the final prediction. The standard deviation of these 500 predictions can approximate the model’s internal confidence in its prediction, and is visualized in the prediction histogram in Figures 1, 3 and S7, the last of which illustrates the entirety of the processing steps performed on an input spectrum.

Experimental EELS

To validate the utility of this model on experimental data, experimental EELS spectra of standard reference samples were measured, including Cu metal, Cu₂O and CuO. Cu metal was purchased from Sigma-Aldrich with 99.999% purity. Cu₂O and CuO were purchased from Sigma-Aldrich with 99.99% purity. The Cu₂O sample was measured using a vacuum holder to prevent oxidation. However, the Cu metal sample was not delivered in a vacuum sealed container, and under the assumption that surface oxidation had already occurred, a vacuum holder was not used for this sample.

Using the TEAM I microscope, a double-corrected Thermo Fisher Titan microscope, we acquired monochromated reference data for these samples at roughly 0.2 meV resolution. Data were collected at 300kV with a semi-convergence angle of 17 mrad and a collection angle of 82 mrad. All data was collected using a Gatan Continuum spectrometer equipped with a K3-IS detector operated in electron counting mode. Spectra were baseline subtracted using the GMS Digital Micrograph software package, and spectra were taken using dual EELS to dynamically remove shifts in the reference elastic energy and deconvolved with the simultaneously measured zero-loss region to mitigate artifacts from electrons experiencing multiple scattering events. The deconvolution of multiple scattering is essential to ensure the experimental EELS spectra are comparable to XAS.

Data and Code Availability

The spectral dataset and the code to generate and analyze the random forest model presented in this study are available upon request.

Author Contributions

SPG took the experimental data, generated the simulated XAS dataset, conducted the machine learning training and analysis and wrote the manuscript. DL provided training and expertise necessary to generate the simulated dataset. JC provided experimental EELS knowledge, microscope training, led the collaboration and designed the scope of this work. All authors read, edited and approved the final manuscript.

Acknowledgment

This work was primarily funded by the US Department of Energy in the program “4D Camera Distillery: From Massive Electron Microscopy Scattering Data to Useful Information with AI/ML.” Work at the Molecular Foundry was supported by the Office of Science, Office of Basic Energy Sciences, of the U.S. Department of Energy under Contract No. DE-AC02-05CH11231. This research used Theory and Computation resources of the Center for Functional Nanomaterials (CFN), which is a U.S. Department of Energy Office of Science User Facility, at Brookhaven National Laboratory under Contract No. DE-SC0012704. The training and instrumentation support necessary to operate the TEAM I microscope and acquire the experimental EELS data presented in this work was provided by Dr Chengyu Song.

References

- [1] Dalle, K.E., Warnan, J., Leung, J.J., Reuillard, B., Karmel, I.S., Reisner, E.: Electro- and Solar-Driven Fuel Synthesis with First Row Transition Metal Complexes. *Chemical Reviews* **119**(4), 2752–2875 (2019) <https://doi.org/10.1021/acs.chemrev.8b00392>

- [2] Mccusker, J.K.: Electronic structure in the transition metal block and its implications for light harvesting. *Science* **363**, 484–488 (2019)
- [3] Johnstone, T.C., Suntharalingam, K., Lippard, S.J.: Third row transition metals for the treatment of cancer. *Philosophical Transactions of the Royal Society A: Mathematical, Physical and Engineering Sciences* **373**(2037) (2015) <https://doi.org/10.1098/rsta.2014.0185>
- [4] Batson, P.E.: Simultaneous STEM imaging and electron energy-loss spectroscopy with atomic-column sensitivity. *Nature* **366**, 727–728 (1993)
- [5] Browning, N.D., Chisholm, M.F., Pennycook, S.J.: Atomic-resolution chemical analysis using a scanning transmission electron microscope. *Nature* **366**, 143–146 (1993)
- [6] Yang, G., Cheng, S., Li, C., Zhong, J., Ma, C., Wang, Z., Xiang, W.: Investigation of the oxidation states of Cu additive in colored borosilicate glasses by electron energy loss spectroscopy. *Journal of Applied Physics* **116**(22) (2014) <https://doi.org/10.1063/1.4903955>
- [7] Gazquez, J., Sanchez-Santolino, G., Biskup, N., Roldan, M.A., Cabero, M., Pennycook, S.J., Varela, M.: Applications of STEM-EELS to complex oxides. Elsevier Ltd (2017). <https://doi.org/10.1016/j.mssp.2016.06.005>
- [8] Kociak, M., Stephan, O.: Mapping plasmons at the nanometer scale in an electron microscope. *Royal Society of Chemistry* (2014). <https://doi.org/10.1039/c3cs60478k>
- [9] Bai, Y., Wu, Y., Zhou, X., Ye, Y., Nie, K., Wang, J., Xie, M., Zhang, Z., Liu, Z., Cheng, T., Gao, C.: Promoting nickel oxidation state transitions in single-layer NiFeB hydroxide nanosheets for efficient oxygen evolution. *Nature Communications* **13**(1) (2022) <https://doi.org/10.1038/s41467-022-33846-0>
- [10] Kubin, M., Guo, M., Kroll, T., Lochel, H., Kallman, E., Baker, M.L., Mitzner, R., Gul, S., Kern, J., Fohlich, A., Erko, A., Bergmann, U., Yachandra, V., Yano, J., Lundberg, M., Wernet, P.: Probing the oxidation state of transition metal complexes: a case study on how charge and spin densities determine Mn L-edge X-ray absorption energies. *Chemical Science* **9**(33), 6813–6829 (2018) <https://doi.org/10.1039/c8sc00550h>
- [11] Henderson, G.S., Groot, F.M.F., Moulton, B.J.A.: X-ray absorption near-edge structure (XANES) spectroscopy. In: *Spectroscopic Methods in Mineralogy and Materials Sciences*, pp. 75–138. De Gruyter, ??? (2014). <https://doi.org/10.2138/rmg.2014.78.3>
- [12] Yu, L., Li, M., Wen, J., Amine, K., Lu, J.: (S)TEM-EELS as an advanced characterization technique for lithium-ion batteries. *Royal Society of Chemistry* (2021).

<https://doi.org/10.1039/d1qm00275a>

- [13] Batson, P.E., Dellby, N., Krivanek, O.L.: Sub-ångstrom resolution using aberration corrected electron optics. *Nature* **418**(6898), 617–620 (2002) <https://doi.org/10.1038/nature00972>
- [14] Hart, J.L., Lang, A.C., Li, Y., Shahrezaei, S., Alix-Williams, D.D., Falk, M.L., Mathaudhu, S.N., Frenkel, A.I., Taheri, M.L.: Revealing local order via high energy EELS. *Materials Today Nano* **21** (2023) <https://doi.org/10.1016/j.mtnano.2022.100298>
- [15] Akgul, G., Akgul, F.A., Ufuktepe, Y.: Investigation of thickness dependence on electronic structures of iron and nickel thin films by L-edge X-ray absorption spectroscopy. *Vacuum* **99**, 211–215 (2014) <https://doi.org/10.1016/j.vacuum.2013.06.003>
- [16] Keast, V.J., Scott, A.J., Brydson, R., Williams, D.B., Bruley, J.: Electron energy-loss near-edge structure a tool for the investigation of electronic structure on the nanometre scale. *Journal of Microscopy* **203**, 135–175 (2001)
- [17] Cressey, G., Henderson, C.M.B., Van Der Laan, G.: Use of L-edge X-ray Absorption Spectroscopy to Characterize Multiple Valence States of 3d Transition Metals; a New Probe for Mineralogical and Geochemical Research. *Phys Chem Minerals* **20**, 111–119 (1993)
- [18] Zhang, S., Livi, K.J.T., Gaillot, A.C., Stone, A.T., Veblen, D.R.: Determination of manganese valence states in (Mn³⁺, Mn⁴⁺) minerals by electron energy-loss spectroscopy. *American Mineralogist* **95**(11-12), 1741–1746 (2010) <https://doi.org/10.2138/am.2010.3468>
- [19] Van Aken, P.A., Liebscher, B.: Quantification of ferrous/ferric ratios in minerals: New evaluation schemes of Fe L23 electron energy-loss near-edge spectra. *Physics and Chemistry of Minerals* **29**(3), 188–200 (2002) <https://doi.org/10.1007/s00269-001-0222-6>
- [20] Laurence A. J. Garvie, Peter R. Buseck: Ratios of ferrous to ferric iron from nanometre-sized areas in minerals. *letters to nature* **396**, 667–670 (1998)
- [21] Grioni, M., Van Acker, J.F., Czyzyk, M.T., Fuggle, J.C.: Unoccupied electronic structure and core-hole effects in the x-ray-absorption spectra of Cu₂O. *PHYSICAL REVIEW B* **45**, 3309–3318 (1992)
- [22] Shang, H., Zhou, X., Dong, J., Li, A., Zhao, X., Liu, Q., Lin, Y., Pei, J., Li, Z., Jiang, Z., Zhou, D., Zheng, L., Wang, Y., Zhou, J., Yang, Z., Cao, R., Sarangi, R., Sun, T., Yang, X., Zheng, X., Yan, W., Zhuang, Z., Li, J., Chen, W., Wang, D., Zhang, J., Li, Y.: Engineering unsymmetrically coordinated Cu-S₁N₃ single atom sites with enhanced oxygen reduction activity. *Nature Communications* **11**(1)

(2020) <https://doi.org/10.1038/s41467-020-16848-8>

- [23] Groot, F.D.: Multiplet effects in X-ray spectroscopy (2005). <https://doi.org/10.1016/j.ccr.2004.03.018>
- [24] Timoshenko, J., Lu, D., Lin, Y., Frenkel, A.I.: Supervised Machine-Learning-Based Determination of Three-Dimensional Structure of Metallic Nanoparticles. *Journal of Physical Chemistry Letters* **8**(20), 5091–5098 (2017) <https://doi.org/10.1021/acs.jpcelett.7b02364>
- [25] Carbone, M.R., Yoo, S., Topsakal, M., Lu, D.: Classification of local chemical environments from x-ray absorption spectra using supervised machine learning. *Physical Review Materials* **3**(3) (2019) <https://doi.org/10.1103/PhysRevMaterials.3.033604>
- [26] Torrisi, S.B., Carbone, M.R., Rohr, B.A., Montoya, J.H., Ha, Y., Yano, J., Suram, S.K., Hung, L.: Random forest machine learning models for interpretable X-ray absorption near-edge structure spectrum-property relationships. *npj Computational Materials* **6**(1) (2020) <https://doi.org/10.1038/s41524-020-00376-6>
- [27] Zheng, C., Mathew, K., Chen, C., Chen, Y., Tang, H., Dozier, A., Kas, J.J., Vila, F.D., Rehr, J.J., Piper, L.F.J., Persson, K.A., Ong, S.P.: Automated generation and ensemble-learned matching of X-ray absorption spectra. *npj Computational Materials* **4**(1) (2018) <https://doi.org/10.1038/s41524-018-0067-x>
- [28] Bonnet, N.: Multivariate statistical methods for the analysis of microscope image series: applications in materials science. *Journal of Microscopy* **190**, 2–18 (1998)
- [29] Noel Bonnet: Artificial Intelligence and Pattern Recognition Techniques in Microscope Image Processing and Analysis. *Advances in imaging and electron physics* **114**, 1–77 (2000)
- [30] Bosman, M., Watanabe, M., Alexander, D.T.L., Keast, V.J.: Mapping chemical and bonding information using multivariate analysis of electron energy-loss spectrum images. *Ultramicroscopy* **106**(11-12 SPEC. ISS.), 1024–1032 (2006) <https://doi.org/10.1016/j.ultramic.2006.04.016>
- [31] Kotula, P.G., Keenan, M.R.: Application of multivariate statistical analysis to STEM X-ray spectral images: Interfacial analysis in microelectronics. In: *Microscopy and Microanalysis*, vol. 12, pp. 538–544 (2006). <https://doi.org/10.1017/S1431927606060636>
- [32] Cueva, P., Hovden, R., Mundy, J.A., Xin, H.L., Muller, D.A.: Data processing for atomic resolution electron energy loss spectroscopy. In: *Microscopy and Microanalysis*, vol. 18, pp. 667–675 (2012). <https://doi.org/10.1017/S1431927612000244>

- [33] Bonnet, N., Nuzillard, D.: Independent component analysis: A new possibility for analysing series of electron energy loss spectra. *Ultramicroscopy* **102**(4), 327–337 (2005) <https://doi.org/10.1016/j.ultramic.2004.11.003>
- [34] Bosman, M., Keast, V.J., García-Muñoz, J.L., D’Alfonso, A.J., Findlay, S.D., Allen, L.J.: Two-dimensional mapping of chemical information at atomic resolution. *Physical Review Letters* **99**(8) (2007) <https://doi.org/10.1103/PhysRevLett.99.086102>
- [35] Li, R., Jiang, X., Zhou, C., Topsakal, M., Nykypanchuk, D., Attenkofer, K., Stacchiola, D.J., Hybertsen, M.S., Stavitski, E., Qu, X., Lu, D., Liu, M.: Deciphering phase evolution in complex metal oxide thin films via high-throughput materials synthesis and characterization. *Nanotechnology* **34**(12) (2023) <https://doi.org/10.1088/1361-6528/acad09>
- [36] Chatzidakis, M., Botton, G.A.: Towards calibration-invariant spectroscopy using deep learning. *Scientific Reports* **9**(1) (2019) <https://doi.org/10.1038/s41598-019-38482-1>
- [37] Ji, Z., Hu, M., Xin, H.L.: MnEdgeNet for accurate decomposition of mixed oxidation states for Mn XAS and EELS L_{2,3} edges without reference and calibration. *Scientific Reports* **13**(1), 14132 (2023) <https://doi.org/10.1038/s41598-023-40616-5>
- [38] del-Pozo-Bueno, D., Kepaptsoglou, D., Peiró, F., Estradé, S.: Comparative of machine learning classification strategies for electron energy loss spectroscopy: Support vector machines and artificial neural networks. *Ultramicroscopy* **253**, 113828 (2023) <https://doi.org/10.1016/j.ultramic.2023.113828>
- [39] Jain, A., Ong, S.P., Hautier, G., Chen, W., Richards, W.D., Dacek, S., Cholia, S., Gunter, D., Skinner, D., Ceder, G., Persson, K.A.: Commentary: The materials project: A materials genome approach to accelerating materials innovation. American Institute of Physics Inc. (2013). <https://doi.org/10.1063/1.4812323>
- [40] Chen, Y., Chen, C., Zheng, C., Dwaraknath, S., Horton, M.K., Cabana, J., Rehr, J., Vinson, J., Dozier, A., Kas, J.J., Persson, K.A., Ong, S.P.: Database of ab initio L-edge X-ray absorption near edge structure. *Scientific Data* **8**(1) (2021) <https://doi.org/10.1038/s41597-021-00936-5>
- [41] R.F. Egerton: *Electron Energy-Loss Spectroscopy in the Electron Microscope*, 3rd edn. Springer, ??? (2011)
- [42] Moreno, M.S., Jorissen, K., Rehr, J.J.: Practical aspects of electron energy-loss spectroscopy (EELS) calculations using FEFF8. *Micron* **38**(1), 1–11 (2007) <https://doi.org/10.1016/j.micron.2006.03.011>
- [43] Bhagat, M., Anand, R., Sharma, P., Rajput, P., Sharma, N., Singh, K.:

- Review—Multifunctional Copper Nanoparticles: Synthesis and Applications. *ECS Journal of Solid State Science and Technology* **10**(6), 063011 (2021) <https://doi.org/10.1149/2162-8777/ac07f8>
- [44] Gawande, M.B., Goswami, A., Felpin, F.X., Asefa, T., Huang, X., Silva, R., Zou, X., Zboril, R., Varma, R.S.: Cu and Cu-Based Nanoparticles: Synthesis and Applications in Catalysis. American Chemical Society (2016). <https://doi.org/10.1021/acs.chemrev.5b00482>
- [45] Laffont, L., Wu, M.Y., Chevallier, F., Poizot, P., Morcrette, M., Tarascon, J.M.: High resolution EELS of Cu-V oxides: Application to batteries materials. *Micron* **37**(5), 459–464 (2006) <https://doi.org/10.1016/j.micron.2005.11.007>
- [46] John J. Rehr, Joshua J. Kas, Fernando D. Vila, Micah P. Prange, Kevin Jorissen: Parameter-free calculations of X-ray spectra with FEFF9. *Physical Chemistry Chemical Physics* **12**, 5503–5513 (2010)
- [47] Carbone, M.R., Meng, F., Vorwerk, C., Maurer, B., Peschel, F., Qu, X., Stavitski, E., Draxl, C., Vinson, J., Lu, D.: Lightshow: a Python package for generating computational x-ray absorption spectroscopy input files. *Journal of Open Source Software* **8**(87), 5182 (2023) <https://doi.org/10.21105/joss.05182>
- [48] Pedregosa, F., Michel, V., Grisel OLIVIERGRISEL, O., Blondel, M., Prettenhofer, P., Weiss, R., Vanderplas, J., Cournapeau, D., Pedregosa, F., Varoquaux, G., Gramfort, A., Thirion, B., Grisel, O., Dubourg, V., Passos, A., Brucher, M., Perrot and Édouardand, M., Duchesnay, a., Duchesnay EDOUARDDUCHESNAY, F.: Scikit-learn: Machine Learning in Python Gaël Varoquaux Bertrand Thirion Vincent Dubourg Alexandre Passos PEDREGOSA, VAROQUAUX, GRAMFORT ET AL. Matthieu Perrot. *Journal of Machine Learning Research* **12**, 2825–2830 (2011)
- [49] Virtanen, P., Gommers, R., Oliphant, T.E., Haberland, M., Reddy, T., Cournapeau, D., Burovski, E., Peterson, P., Weckesser, W., Bright, J., Walt, S.J., Brett, M., Wilson, J., Millman, K.J., Mayorov, N., Nelson, A.R.J., Jones, E., Kern, R., Larson, E., Carey, C.J., Polat, .I., Feng, Y., Moore, E.W., VanderPlas, J., Laxalde, D., Perktold, J., Cimrman, R., Henriksen, I., Quintero, E.A., Harris, C.R., Archibald, A.M., Ribeiro, A.H., Pedregosa, F., Mulbregt, P., SciPy 1.0 Contributors: SciPy 1.0: Fundamental Algorithms for Scientific Computing in Python. *Nature Methods* **17**, 261–272 (2020) <https://doi.org/10.1038/s41592-019-0686-2>

Supporting Information For Prediction of the Cu Oxidation State from EELS and XAS Spectra Using Supervised Machine Learning

Samuel P. Gleason^{1,2*}, Deyu Lu³ and Jim Ciston^{1*}

¹National Center for Electron Microscopy Facility, Molecular Foundry, Lawrence Berkeley National Laboratory, Berkeley, CA, USA.

²Department of Chemistry, University of California, Berkeley, 94720, CA, USA.

³Center for Functional Nanomaterials, Brookhaven National Laboratory, Street, Upton, 100190, NY, USA.

*Corresponding author(s). E-mail(s): smglsn12@berkeley.edu; jciston@lbl.gov;

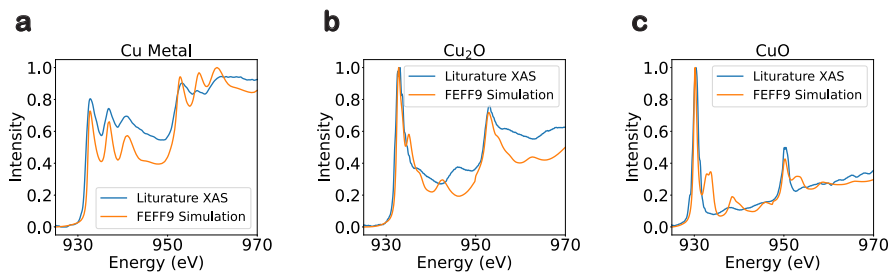


Fig. S1 Comparison of the simulated FEFF9 spectra to literature XAS spectra extracted from [21]. All three comparisons show good qualitative agreement between the experimental and simulated Cu XAS spectra and have been shifted on their energy axis to allow the peaks to align correctly. The Cu(0) spectrum (a) was shifted by -0.9 eV while the other two (b,c) were shifted by -1.2 eV

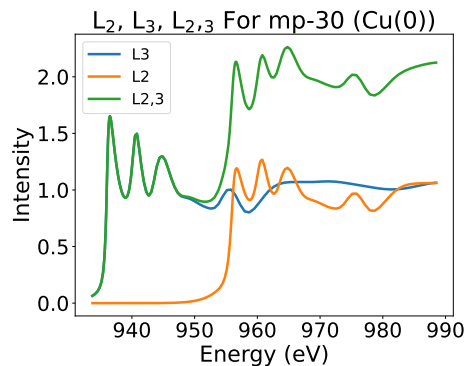


Fig. S2 Illustration of how $L_{2,3}$ spectra are created from the individual L_2 and L_3 spectra. Post interpolation to place the L_2 and L_3 spectra on the same 0.1 eV energy axis, the two spectra are simply summed together to produce the $L_{2,3}$ spectrum.

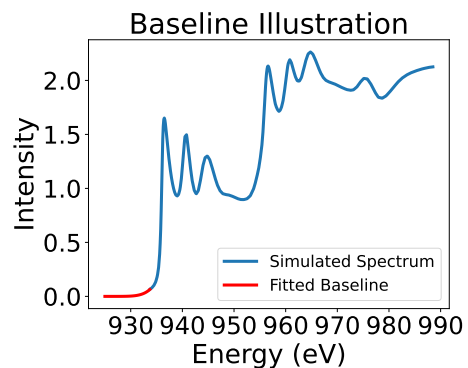


Fig. S3 How the pre-edge of each spectrum is scaled so all spectra start at the same energy and have all their intensities start at zero. The final result is a set of spectra running from 925-970 eV with their first values at [925, 0].

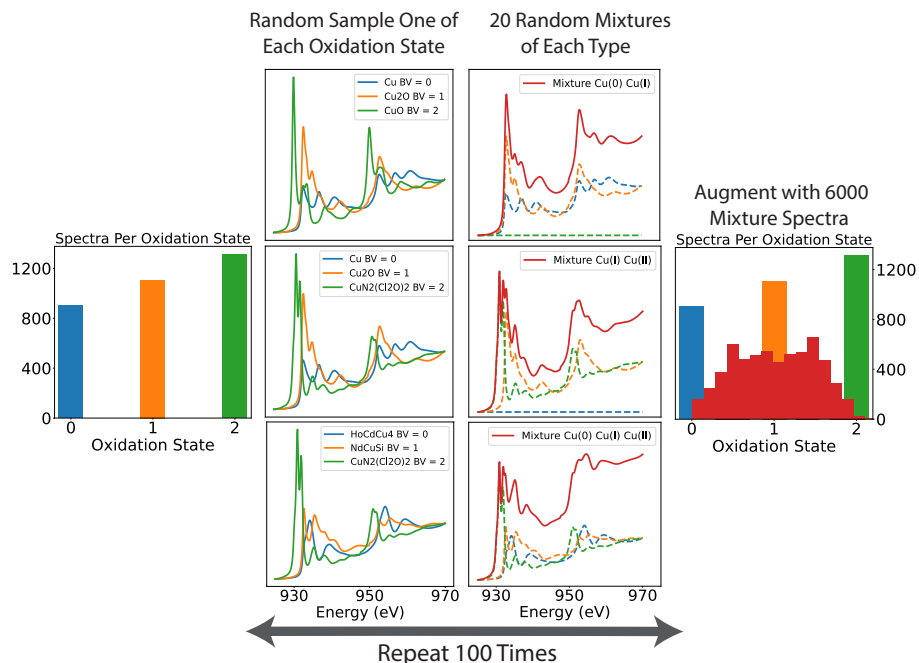


Fig. S4 Illustration of data augmentation with simulated mixed valence samples. 100 random spectra are sampled from the full dataset (a,b), and then 20 combinations of Cu(0) and Cu(I) are computed for randomly generated mixture values (c). This process is then repeated two additional times for mixtures of Cu(I) and Cu(II) (d,e), and mixtures of Cu(0), Cu(I) and Cu(II) (f,g). This produces a set of 6000 mixture spectra which fully fills out the spaces between the integer spectra values (h).

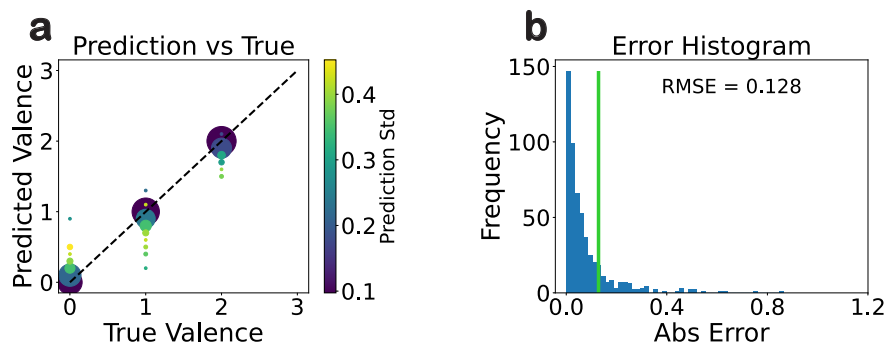


Fig. S5 Model accuracy on the integer spectra used to build the mixture dataset. The spot size in (a) corresponds to the number of spectra at that set of values, and the color corresponds to the prediction standard deviation. In (b), the green vertical line indicates the RMSE.

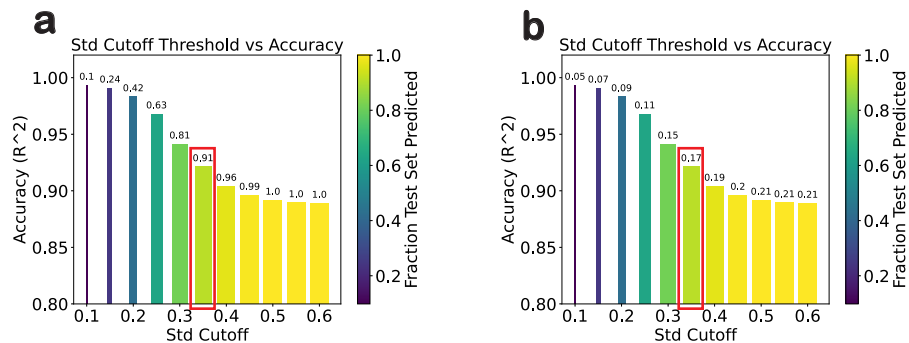


Fig. S6 How using specific values of the standard deviation as a threshold to filter out predictions that are highly uncertain changes the percentage of the test set retained (a text above bars) and the RMSE of the retained test set (b text above bars). The red rectangle shows a threshold value of 0.35, where 91% of the test set is retained. 9% is discarded because those data points have standard deviations higher than 0.35. When the remaining 91% of the test set is evaluated, the RMSE falls from 0.21 to 0.17. The color and width of the bars corresponds to the percentage of the test set predicted when that standard deviation threshold is selected. The height of the bars corresponds to the R^2 of that standard deviation threshold.

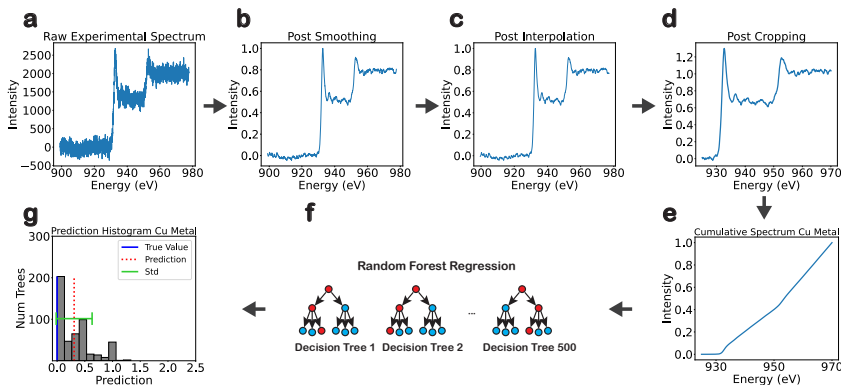


Fig. S7 An outline of every processing step for a raw experimental spectrum predicted by this model. After the raw spectrum is taken (a) the spectrum is smoothed with a Savitzky-Golay filter (b). The spectrum is then interpolated onto a 0.1 eV scale (c) and cropped to run from an energy axis of 925-970 eV (d). The spectrum is transformed into a cumulative spectrum (e) and inputted into the random forest model (f). This results in the outputted prediction (g), which includes the final prediction (red vertical line) full predictions across all 500 decision trees (grey bars) and standard deviation (green horizontal line).

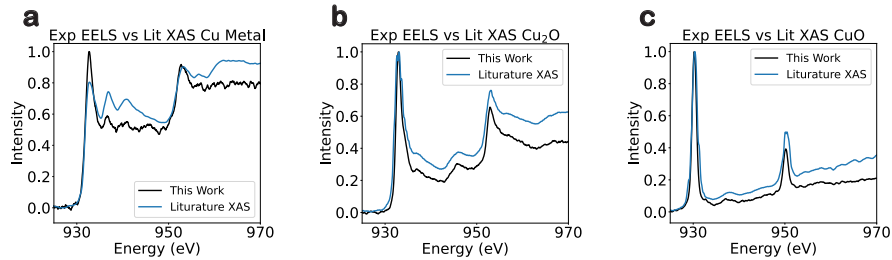


Fig. S8 Comparison of Cu(0) (a), Cu(I) (b) and Cu(II) (c) from [21] and our home institution. The sharp first peak in (a) and its higher intensity relative to the higher energy peaks clearly indicates the presence of Cu(I), as shown in (b).

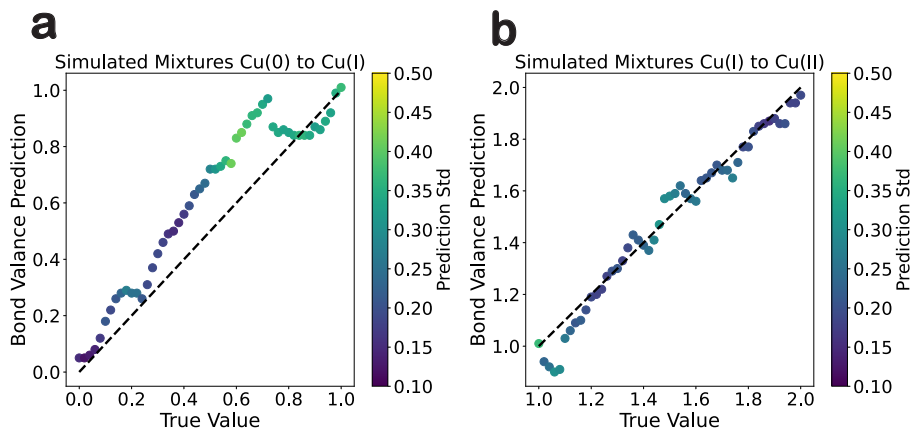


Fig. S9 Accuracy of the RF model on simulated mixture test spectra. (a) corresponds to mixtures of Cu(0) and Cu(I) and (b) shows mixtures of Cu(I) and Cu(II). The spectra selected for this visualization are mixtures of Cu(0), Cu₂O and CuO. The color of the dots corresponds to the prediction standard deviation. The dashed line indicates the location of a perfect prediction.

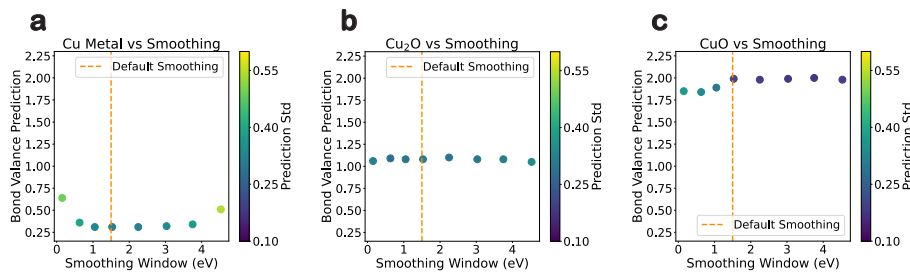


Fig. S10 How various amounts of smoothing our experimental standard samples impacts the prediction for Cu(0) (a), Cu(I) (b), and Cu(II) (c). The vertical line indicates the default smoothing condition, window size of 1.5 eV.